01 Aug 2004

Anticipating EMI and On-Board Interference in Automotive Platforms

Shishuang Sun

Geping Liu

David Pommerenke
Missouri University of Science and Technology, davidjp@mst.edu

James L. Drewniak
Missouri University of Science and Technology, drewniak@mst.edu

et. al. For a complete list of authors, see https://scholarsmine.mst.edu/ele_comeng_facwork/892

Recommended Citation

S. Sun et al., "Anticipating EMI and On-Board Interference in Automotive Platforms," *Proceedings of the IEEE International Symposium on Electromagnetic Compatibility (2004, Santa Clara, CA)*, vol. 3, pp. 792-797, Institute of Electrical and Electronics Engineers (IEEE), Aug 2004.
The definitive version is available at https://doi.org/10.1109/ISEMC.2004.1349923

Anticipating EMI and On-Board Interference in Automotive Platforms

Shishuang Sun, Geping Liu, David J. Pommerenke, James L. Drewniak
Electromagnetic Compatibility Laboratory
Department of Electrical and Computer Engineering
University of Missouri-Rolla
Rolla, MO 65401, USA
sspmc@umr.edu, geping@umr.edu

Richard W. Kautz, Chingchi Chen
Ford Motor Company
Dearborn, MI, 48121-2053, USA
rkautz1@ford.com, and cchen4@ford.com

Abstract— **A dual-step MTL / FDTD strategy is proposed for anticipating full-vehicle level EMI. In the first step, the current distribution along a cable bundle connecting to electronic modules on an automotive platform is calculated using multi-conductor transmission-line (MTL) models. In order to account for common-mode discontinuities on the vehicle chassis, e.g., slots, 3D full-wave modeling (FDTD) is used to determine radiation impedances, which are thereafter incorporated in the MTL models for compensating the radiation power loss. In the second step, the obtained currents are implemented as impressed current sources in full-vehicle full-wave modeling using an FDTD multi-wire subcelluar algorithm. Thus, the full-vehicle emissions from the automotive harness and the common-mode discontinuities of the vehicle chassis can be predicted. The effectiveness and limitation of this approach have been demonstrated in a controlled laboratory environment.**

Keywords - Multi-conductor transmission line (MTL); FDTD multi-wire subcelluar algorithm; common-mode current; automotive EMC

I. INTRODUCTION

Electromagnetic interference (EMI) caused by electronic modules and the complexity of wire bundles and the vehicle chassis might prevent commercial vehicles from satisfying stringent EMC criteria. In addition, wire bundles with their small cross-sectional dimensions compared to larger car body dimensions limit the application of 3D full-wave analysis for electromagnetic compatibility (EMC) design. Indeed, the mesh size required to describe wires inside bundles is too small, and leads to an enormous demand on computer memory. A method of using hybrid MTL / BEM was applied to attack the complex problems of automotive EMC in [1], [2]. A proposed methodology in [3] consisted of calculating the incident fields with 3D FDTD modeling and the coupling on cables with an MTL network model. In addition, Holland's FDTD thin wire formalism [4] was generalized to a multi-wire formalism [5] that can take account of bundles composed of parallel wires, without limitation on the spacing between the wires inside the bundles. In [6], [7], Holland's thin wire algorithm was extended to allow modeling an arbitrarily located and oriented wire with respect to the Cartesian FDTD grid. In this paper, a semi full-wave approach combining MTL and FDTD modeling is proposed for automotive applications. As compared to the full-wave multi-wire model in [5], the MTL model is especially suitable to calculate the current distribution along the complex automotive harness on the vehicle chassis because of its simplicity and accuracy, while full-wave FDTD modeling is suitable for calculating electromagnetic fields. In Section II, a dual-step MTL/FDTD procedure is briefly described, and in Section III an FDTD multi-wire subcelluar algorithm is introduced. In Section IV, a test setup in a controlled laboratory environment is used to demonstrate the effectiveness and limitations of the procedure. Finally, the procedure is summarized in Section V.

II. DUAL-STEP MTL/FDTD PROCEDURE

To anticipate full-vehicle level EMI, a suitable approach must include the transmission-line mode propagation in a cable bundle, as well as including the radiating (common) mode, with current that returns on the vehicle chassis. The common-mode current ultimately illuminates the vehicle, and contributes to interference. The approach should include both MTL modeling for the cable bundle, as well as full-wave modeling for the electromagnetic scattering problem that characterizes EMI. Thus, a dual-step MTL / FDTD procedure can be used to reflect the underlying physics.

In the first step, an MTL model is used to calculate current distributions along automotive harnesses under the assumption that their transverse dimensions are much smaller than the minimum wavelength of interest, i.e., a TEM or quasi-TEM mode [8]. A cable bundle installed in a vehicle is segmented into equivalent 2D cross section geometries, which are translationally invariant along the particular partition length. A quasi-static 2D field solver is used to extract the per-unit-length (p. u. l.) transmission-line matrices of inductance, capacitance, conductance, and resistance, for each translationally invariant segment. A time- or frequency- domain formulation for the MTL equations, i.e., the coupled partial differential equations, can provide good estimates for currents and voltages on the MTL in the quasi-TEM assumption [8]. Herein the pin-by-pin module-level noise sources and impedances, which are necessary terminal conditions for an MTL model, are assumed to be characterized with module-level measurements, or

0-7803-8443-1/04/$20.00 © IEEE.

suitable alternatives. This topic is outside the discussion scope of this paper.

In a typical case of harnesses on an automotive platform, the TEM or quasi-TEM assumption can be globally satisfied, however, complicated conversions (mode conversion, or mode coupling) from the transmission-line mode to a radiating mode may still result when the harnesses are placed across some common-mode discontinuities on the chassis, e.g., slots or apertures. These unintentional mode-conversions that may impair the vehicle-level EMC performance, cannot be simply characterized through 2D quasi-static field solvers. To account for the common-mode discontinuities in the first-step MTL model, an additional full-wave model has to be used for extracting physics-based lumped radiation impedances, or equivalent S-parameter networks. These equivalent radiation impedances or S-parameter networks actually reflect the illumination physics of common-mode currents on the automotive platform, and compensate radiation power loss that cannot be considered in traditional transmission-line models. However, when the height of cable bundles over the chassis is comparable to or greater than one tenth of the shortest wavelength, the radiation loss caused by the non-TEM modes (or antenna mode) cannot be compensated in the standard MTL model, and consequently influence the accuracy of current distributions along the bundles.

In the second step, the current distributions obtained from the first-step MTL model are applied in a subsequent FDTD model (Maxwell equations) as impressed current sources, i.e., Maxwellian sources that are transparent to electromagnetic fields. The PEC boundary conditions of conductors and dielectric properties of insulation materials have been considered in the calculation of the per-unit-length inductance and capacitance matrices. In the 3D FDTD model, the time increment Δt is identical to that of the Gaussian or modulated Gaussian excitation source in the MTL model. At every time step $t = n\Delta t$, where n is an integer, the recorded currents on each MTL segment are partitioned into impressed current densities by using reasonable interpolation techniques. Then the rectangular components of the vector electric and magnetic fields are updated in an FDTD Yee grid [9]. An FDTD multi-wire subcelluar algorithm reflecting the coupling mechanism between the MTL currents and electric fields will be described in Section III in detail.

III. A 3D FDTD MULTI-WIRE SUBCELLUAR ALGORITHM GIVEN DISTRIBUTED MAXWELLIAN CURRENT SOURCES

As long as the first-step MTL model, or a suitable alternative, provides the current distributions along cable bundles, a generalized FDTD multi-wire subcelluar algorithm is proposed for incorporating these current sources and further calculating the EM fields. This multi-wire formalism overcomes the limitation of the FDTD thin wire subcelluar algorithms [4], i.e., the separation between parallel wires, which must be at least on the order of the FDTD cell size. The algorithm proposed in this paper is much simpler than the full-wave multi-wire model [5], and has the potential to handle arbitrarily located and oriented cable bundles with respect to the Cartesian grid.

Maxwell's curl equations that describe time-varying electromagnetic fields in a 3D computational domain can be numerically solved by the FDTD method in the Yee grid, i.e., a structured grid composed of rectangular cells [9], [10]. According to the leap-frog scheme, time is discretized into equal time intervals Δt, and the electric and the magnetic fields are calculated at different time instants, $t = n\Delta t$ and $t = (n+1/2)\Delta t$, respectively, where n is the iteration number. By applying the finite-difference scheme, Maxwell's curl equations become

$$\vec{H}^{n+1/2} = \vec{H}^{n-1/2} - \left(\frac{\Delta t}{\mu}\right)\nabla \times \vec{E}^{n}, \tag{1}$$

$$\vec{E}^{n+1} = \frac{2\varepsilon - \sigma\Delta t}{2\varepsilon + \sigma\Delta t}\vec{E}^{n} + \frac{2\Delta t}{2\varepsilon + \sigma\Delta t}(\nabla \times \vec{H}^{n+1/2} - \vec{J}^{n+1/2}), \tag{2}$$

where $n+1/2$ and $n+1$ refer to the time instants $t = (n+1/2)\Delta t$ and $t = (n+1)\Delta t$, respectively. According to the basic FDTD notation, the rectangular components of the vector electric and magnetic fields are calculated at different points of the FDTD structured grid.

Given the distributed current information, the coupling back to the 3D electric field equation (2) is through the impressed source term $\vec{J}$. For simplicity, a single wire case is used for demonstration first. In general, this wire is not aligned with the edges in the grid, and the current is distributed as current densities for the surrounding electric field components. The current along the wire can be expanded in basis functions as [7]

$$I(\xi) = \sum_{j} I_j \Phi_j(\xi) \tag{3}$$

where ξ is an arbitrary point on the wire, Φ_j is a discrete weighting function equal to one when ξ is located on segment j, and zero when ξ is located on all other segments, and I_j is the known amplitude of the current on wire segment j. Therefore, the current density $\vec{J}_j(r)$ at one point inside the FDTD cell is expressed as

$$\vec{J}_j(r) = \sum_{j} \frac{I_j \Phi_j(\xi)}{A(r,\xi)} \hat{\xi}_j, \tag{4}$$

where r is a radial distance from the wire, $\hat{\xi}_j$ is the directional vector of the wire segment j, and $A(r, \xi)$ is an appropriate scalar weighting function representing the equivalent area of current distribution. In order to describe the algorithm in a more compact form, finite element method (FEM) notation is used. Consider an FDTD cell (brick element), the side length is Δx, Δy, and Δz in the x-, y-, and z-directions, respectively. Since the tangential electric field component is constant along each edge of the Yee grid, the field components within the element can be expressed as

$$\vec{E}^e = \sum_{i=1}^{12} \vec{N}_i^e E_i^e , \quad (5)$$

where

$$\vec{N}_i^e = N_{xi}^e \hat{x}, \vec{N}_{i+4}^e = N_{yi}^e \hat{y}, \vec{N}_{i+8}^e = N_{zi}^e \hat{z}, i = 1, 2, 3, 4 , (6)$$

and N_{xi}^e, N_{yi}^e, N_{zi}^e are edge basis functions for brick elements [11]. The distributed current density in the direction of *Edge k*, where $k = 1, 2, \ldots 12$, is approximated by [7]

$$J_k^{distrib} = \frac{\int \vec{J}(r) \bullet \vec{N}_k^e(\vec{r}) dV}{\Delta x \Delta y \Delta z} = \frac{\sum_j I_j \int \frac{\Phi_j(\xi) \hat{\xi}_j \bullet \vec{N}_k^e(\vec{r})}{A(r,\xi)} dV}{\Delta x \Delta y \Delta z} . \quad (7)$$

The volume integral is taken over the entire FDTD cell where the wire is embedded. If the single wire is parallel to one edge of the FDTD cell, e.g., the wire is parallel to the x-axis, the weighting function $A(r, \xi)$ is approximately

$$A(r,\xi) = \frac{1}{\Delta y \Delta z} . \quad (8)$$

Given the current information on each wire within a cable bundle, the thin-wire algorithm in (7) is easily generalized to a multi-wire formalism using superposition because the coupling among wires has been considered in the first-step MTL model. The distributed current density in the direction of *Edge k*, where $k = 1, 2, \ldots 12$, is approximated as

$$J_k^{distrib} = \sum_{wire\ i=1}^{n} \frac{\sum_{segment\ j} I_j \int \frac{\Phi_j(\xi) \hat{\xi}_j \bullet \vec{N}_k^e(\vec{r})}{A(r,\xi)} dV}{\Delta x \Delta y \Delta z} . \quad (9)$$

Similarly, if the wire bundle is parallel to one edge of the FDTD cell, (9) can also be simplified. The work in [6], [7] shows that, for an arbitrarily oriented thin wire, it is important to choose an appropriate weighting function $A(r, \xi)$ for achieving better numerical performance.

IV. APPLICATIONS OF THE DUAL-STEP PROCEDURE

A validation experiment was performed in a controlled laboratory environment. The objectives of this experiment were to understand the basic coupling and interference mechanism on a non-ideal metallic ground plane and to demonstrate the effectiveness and limitations of the dual-step procedure. A prototype cable network including a 6-wire ribbon cable, a 2-wire ribbon cable, and a 4-wire ribbon cable was constructed over a large aluminum plate with a 64-cm long by 2-cm wide slot, as shown in Figure 1.

As compared to the large ground plane, the ribbon cables with a small wire separation, approximately 0.127-cm, were actually chosen in such a way that no available 3D numerical code could be efficient in calculating the currents on the cables and electromagnetic interferences in the near and far zones. One end of Wire3 was connected to an SMA jack inside the source box, and all other ends of the wires were terminated with 50Ω SMT resistors inside the source and load boxes. Port1 of a network analyzer (HP8753D) was used to feed Wire3 through the SMA jack, while Port 2 of the network analyzer was connected to a current probe (Fisher F-65), or a lab-made electric field sensor, for the common-mode current and electric field measurements, respectively. The demonstration of the validity of the dual-step procedure was based on comparisons between these measurements and calculations of common-mode currents and electric fields.

In this paper, for the multi-wire ribbon cables over the aluminum plate, the common-mode current is uniquely defined as a current that travels down the cables, but unintentionally returns on the ground plane, and ultimately illuminates the entire ground plane through the slot. In Figure 1, a non-zero common-mode current on the 6-wire ribbon cable excites a complicated radiating mode in the 2-cm wide slot, and this conversion from the non-radiating transmission-line mode is often termed as mode-conversion. This phenomenon has been studied using full-wave simulations in the literature [12], [13]. For an electrically narrow slot, the fundamental EMI mechanism can be characterized as an unintentional EMI noise source driving a slot antenna and resulting in radiation [14]. In Figure 2(a), the EMI noise source V_{cm} exists where a voltage drop causes the EMI slot antenna to be excited, in particular, when the non-zero returning common-mode current illuminates the slot. If an equivalent radiation impedance $Z_{antenna}(f)$ in Figure 2(b) is considered as an inherent property of the entire ground plane, then removing the ribbon cables does not significantly influence its value. A full-wave tool (FDTD herein) can be used to quantify the input impedance of the slot antenna. The entire ground plane without the ribbon cables was fed with a modulated Gaussian-type voltage source with a 50-Ω source resistance between Point 1 and 2, which are approximate vertical projections of the ribbon cable on the two edges of the slot. The aluminum ground plane was modeled with PEC surfaces by setting the tangential electric field to zero. Perfectly-Matched-Layer (PML) absorbing boundary conditions were employed for this model [15]. The antenna impedance of the non-ideal ground plane was computed as

$$Z_{antenna}(f) = \frac{\tilde{V}_{in}(f)}{\tilde{I}_{in}(f)} = \frac{FFT[V_{in}(t)]}{FFT[I_{in}(t)]} , \quad (10)$$

where $V_{in}(t)$ was the voltage drop between Point 1 and 2, and $I_{in}(t)$ was the current flowing through the voltage source. Note that $Z_{antenna}(f)$, $\tilde{V}_{in}(f)$, and $\tilde{I}_{in}(f)$ are complex values.

For the 2D cross sectional geometries shown in Figure 1(b), the dielectric permittivity of cable insulations was experimentally obtained though a time domain reflectometry (TDR). The p. u. l. inductance and capacitance matrices were calculated with a 2D electrostatic approach solving Laplace's equation with a finite element method (FEM), while the conduction and dielectric losses were neglected. A multi-conductor lossy frequency-dependent model in Star-Hspice, i.e., W-element, was employed to simulate the ribbon cables in both the time and frequency domain [16], [17]. The signal discontinuities, e.g., the right angle bends and the branching junction in Figure 1 (a), were approximated as combinations of lumped inductors and capacitors using empirical equations, and embedded between two straight MTL models. To incorporate the common-mode discontinuity, i.e., the frequency-dependent

antenna impedance, into the MTL model, an Hspice G-element (controlled behavior source) was employed according to the specific frequency responses from the full-wave model. This G-element was embedded between two ground planes that are reference nodes of the two segments of the 6-wire ribbon cable respectively, as shown in Figure 3. In this fashion, the standard multi-conductor transmission-line model was augmented to model the typical system-level case, i.e., the coexistence of a local non-TEM and global TEM mode on a chassis. All the ribbon cables were divided into multiple 1-cm long segments, whose lengths are smaller than 1/10 of the shortest wavelength. The currents on each short segment are assumed to be constant. Therefore, the current distributions along the branched cables were determined as the current sources for the subsequent FDTD model.

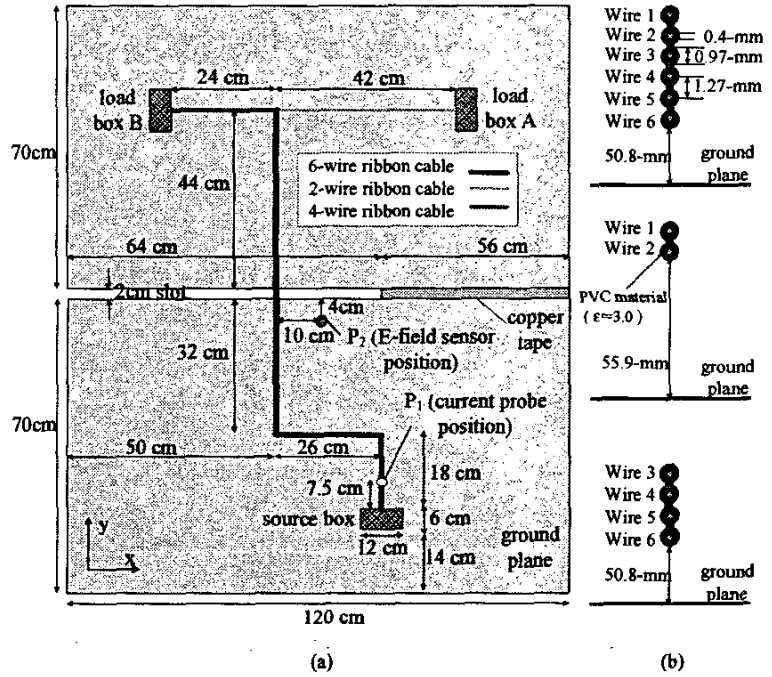

Figure 1. Experimental setup for demonstrating the proposed dual-step MTL / FDTD procedure, (a) top-view of the setup; (b) 2D cross section of the 6-wire ribbon cable, 2-wire ribbon cable, and the 4-wire ribbon cable, respectively.

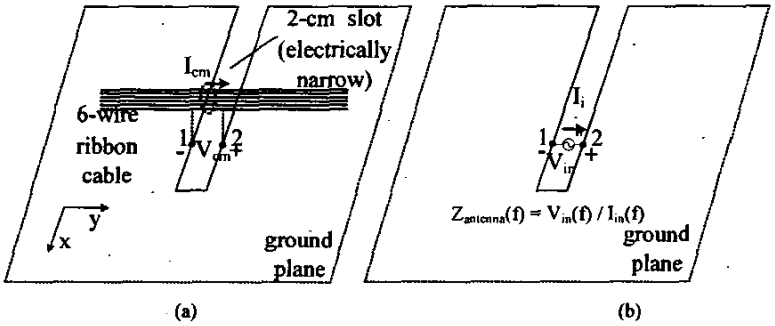

Figure 2. (a) Schematic illustration of the interference physics of the voltage-driven mechanism of the electrically narrow slot; (b) extraction of an EMI antenna impedance through a 3D full-wave model without including the ribbon cables.

To demonstrate the effectiveness and limitation of the enhanced MTL model, the common-mode current of the ribbon cable at P1 as shown in Figure 1 was measured and compared with the results from the dual-step procedure. It is basically a two-port S_{21} measurement using an HP8753D network analyzer. Port 1 of the network analyzer was used to feed the source box through a low-loss cable. A Fischer F-65 current probe connecting to Port 2 of the network analyzer was clamped on the ribbon cable at an arbitrary point marked as P_1 in Figure 1. The measured $|S_{21}|$ is related to the common-mode current on the ribbon cable. For an F-65 probe with a typical flat transfer impedance of 1Ω (±3 dB) from 1 MHz to 1 GHz, a simple yet effective S_{21} through calibration with two broadband attenuators attached to the two low-loss coaxial cables, was used instead. The common-

mode current at P_1 on the 6-wire ribbon cable I_{cm} can be expressed and normalized as

$$\frac{I_{cm}}{V_s} = \frac{S_{21}^{measured}}{2Z_T}, \tag{11}$$

where V_s is the RF source voltage of the network analyzer, Z_T is the transfer impedance of the F-65 probe, 1Ω, and $S_{21}^{measured}$ is the measurement result from the network analyzer. The normalized common-mode currents from the measurement and enhanced MTL model are compared in Figure 4.

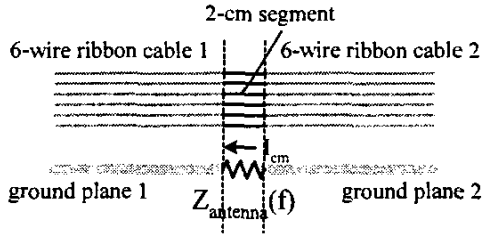

Figure 3. Schematic representation of an enhanced MTL model incorporating the frequency-dependent antenna impedance.

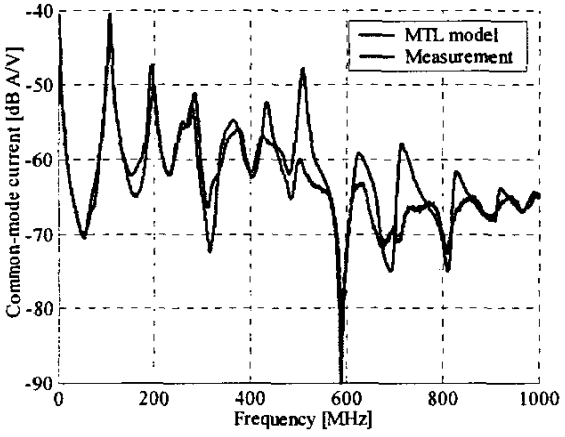

Figure 4. Comparison of the experimental and the first-step MTL modeling results for normalized common-mode current at P1.

In the frequency range below 400 MHz, the height of the ribbon cable over the ground plane, approximately 5-cm, is less than 1/10 of the shortest wavelength, 7.5-cm. Therefore, the TEM or quasi-TEM assumption is satisfied, and the effectiveness of the MTL model is validated with the measurement result. With the increase of the frequency, the quasi-TEM assumption is impaired, and the discrepancies between the MTL model and measurement expand, in particular at the frequency about 500 MHz. Incorporating the antenna impedance into the MTL model approximately compensates the radiation loss from the slot. However, the bends and branching junction of the ribbon cable may exacerbate the radiation loss from the ribbon cables over the ground plane, and this part of radiation loss cannot be considered well in a standard MTL model. This reason directly results in the apparent higher Q-factor of the MTL modeled results as compared to the measurements.

Once the current distributions obtained from the enhanced MTL modeling in the frequency domain was transformed into the time domain, it can be impressed into the second-step FDTD model as Maxwellian sources using the FDTD multi-wire subcelluar algorithm proposed in Section III. In the FDTD modeling, a cell size of 1.0-cm × 1.0-cm × 2.5-cm was employed. In Figure 1, the two aluminum plates, the strip of copper tape, the source and load boxes were modeled as PEC. In this model, the 2-, 4-, and 6-wire ribbon cables are all aligned with edges of FDTD cubic cells, and the general multi-wire formulation can be simplified. As shown in Figure 5, a 1-cm long segment of the 6-wire ribbon cable in the x-direction is incorporated into an FDTD cell. Herein the minimum separation between two wires d_1 is 1.27-mm, and d_2 is 1.28-mm. The FDTD multi-wire subcelluar algorithm allows the cell size, Δy = 1-cm and Δz = 2.5-cm, much larger than d_1 and d_2. The current density at the node $E_x(i+1/2, j, k)$ is obtained by partitioning the MTL currents $I_i(i, j, k)$, $i = 1, 2, 3, \ldots 6$, i.e.,

$$J_x(i+1/2,j,k) = \frac{I_1(i,j,k)}{\Delta y \Delta z}\left(1-\frac{\Delta y'}{\Delta y}\right)\left(\frac{\Delta z'}{\Delta z}\right) + \frac{I_2(i,j,k)}{\Delta y \Delta z}\left(1-\frac{\Delta y'}{\Delta y}\right)\left(\frac{\Delta z'+d}{\Delta z}\right) + \frac{I_3(i,j,k)}{\Delta y \Delta z}\left(1-\frac{\Delta y'}{\Delta y}\right)\left(\frac{\Delta z'+2d}{\Delta z}\right) + \frac{I_4(i,j,k)}{\Delta y \Delta z}\left(1-\frac{\Delta y'}{\Delta y}\right)\left(\frac{\Delta z'+3d}{\Delta z}\right) + \frac{I_5(i,j,k)}{\Delta y \Delta z}\left(1-\frac{\Delta y'}{\Delta y}\right)\left(\frac{\Delta z'+4d}{\Delta z}\right) + \frac{I_6(i,j,k)}{\Delta y \Delta z}\left(1-\frac{\Delta y'}{\Delta y}\right)\left(\frac{\Delta z'+5d}{\Delta z}\right) \tag{12}$$

The distributed current densities at the other three nearest E_x nodes, $J_x(i+1/2, j+1, k)$, $J_x(i+1/2, j, k+1)$, and $J_x(i+1/2, j+1, k+1)$ can also be obtained by using a similar bi-linear interpolation strategy.

The same setup shown in Figure 1 can also be used to validate the electric field results from the dual-step procedure. Still, Port 1 of an HP8753D Network Analyzer was used to feed the source box. An electric field sensor mounted on the ground plane was connected to Port 2 through an RF amplifier for measuring the electric field perpendicular to the ground plane at P_2. The 4-cm × 3-cm × 1-cm rectangular E-field sensor is actually a GaAs impedance converter with active integration, and exhibits a flat frequency response in the frequency range from 2 MHz to 2 GHz with a fluctuation within ±1.5 dB. An S21 through calibration procedure can be used to remove the frequency response of the RF amplifier and cables. Then the measured |S21| result can be directly transformed into the actual electric field at P2 by multiplying the frequency response of the E-field sensor. Figure 6 shows the normalized electric field results at P2 from the dual-step procedure and measurement. In the frequency range below 400 MHz, the modeled result agrees well with the measurement, because the first-step MTL model provides accurate current information for the excitations. With the increase of the

frequency, the underlying assumptions in the procedure are stretched, and the inaccurate current sources also result in apparently higher Q factors of the electric fields as compared to the measured results.

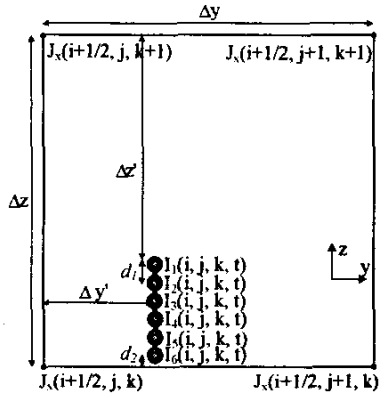

Figure 5. Schematic representation of the FDTD multiwire subcelluar algorithm for the ribbon cable parallel to the x-direction.

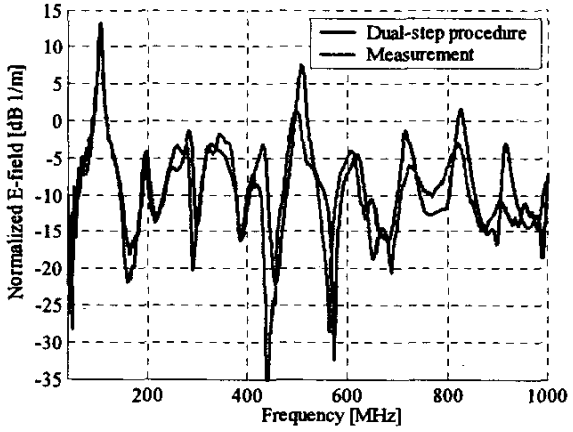

Figure 6. Comparison of experimental and dual-step modeled results for the normalized electric field at P_2.

V. CONCLUSION AND DISCUSSION

The dual-step procedure is actually a semi-full wave strategy that is especially suitable for dealing with a system-level EMI. The first-step MTL model can provide current distributions along the cable bundle, when the common-mode discontinuities on the chassis are reasonably well incorporated into the model. The second-step FDTD model is used to calculate the EM fields after the current distributions are impressed as the excitation source through an FDTD multi-wire subcelluar algorithm. The effectiveness of the procedure is dependent on the accuracy of the current distribution from the first step. For a typical harness on an automotive platform, the dual-step procedure is believed as a suitable strategy for the present frequency range.

REFERENCES

[1] R. Neumayer, A. Stelzer, F. Haslinger, G. Steinmair, M. Troscher, J. Held, B. Unger, R. Weigel, "Numerical EMC simulation for automotive applications", *IEEE EMC Society Newsletter*, No. 197, pp. 30-36, Spring 2003.

[2] R. Neumayer, A. Stelzer, F. Haslinger, J. Held, F. Schinco, R. Weigel, "Continuous simulation of system-level automotive EMC problems", in *Proc. IEEE Int. Symp. Electromagn. Compat.*, pp. 409-413, Aug. 2003.

[3] L. Paletta, J-P. Parmantier, F. Issa, P. Dumas and J-C. Alliot, "Susceptibility analysis of wiring in a complex system combing a 3-D solver and a transmission-line network simulation", *IEEE Trans. Electromagn. Compat.*, vol. 44, no. 2, pp. 309-317, May 2002.

[4] R. Holland and L. Simpson, "Finite-difference analysis of EMP coupling to thin struts and wires", *IEEE Trans. Electromagn. Compat.*, vol. EMC-23, pp. 88-97, May 1981.

[5] J. P. Berenger, "A multiwire formalism for the FDTD method", *IEEE Trans. Electromagn. Compat.*, vol. 42, no. 3, pp. 257-264, Aug. 2002.

[6] G. Ledfelt, "A stable subcell model for arbitrarily oriented thin wires for the FDTD method", *Int. J. Numerical Modeling*, vol. 15, pp. 503-515, 2002.

[7] F. Edelvik, "A new technique for accurate and stable modeling of arbitrarily oriented thin wires in the FDTD method", *IEEE Trans. Electromagn. Compat.*, vol. 45, no. 2, pp. 416-423, May 2003.

[8] C. R. Paul, *Analysis of Multiconductor Transmission Lines*, New York, NY: John Wiley & Sons, Inc., 1994.

[9] K. S. Yee, "Numerical solution of initial boundary value problems involving Maxwell's equations in isotropic media", *IEEE Trans. Antennas Propagat.*, vol. 14, pp. 302-307, May 1966.

[10] A. Taflove, *Computational Electrodynamics: The Finite-Difference Time-Domain Method*, Norwood, MA: Artech House, Inc., 1995.

[11] J. Jin, *The Finite Element Method in Electromagnetics*, 2nd ed. New York: Wiley, 1997.

[12] G. Liang, Y. Liu, and K. K. Mei, "Full-wave analysis of coplanar waveguide and slotline using the time-domain finite-difference method", *IEEE Trans. Microwave Theory Tech.*, vol. 37, pp. 1947-1957, Dec. 1989.

[13] C. Schuster, and W. Fichtner, "Parasitic modes on printed circuit boards and their effects on EMC and signal integrity", *IEEE Trans. Electromagn. Compat.*, vol. 43, no. 4, pp. 416-425, Nov. 2001.

[14] D. M. Hockanson, J. L. Drewniak, T. H. Hubing, T. P. Van Doren, F. Sha, and M. J. Wilhelm, "Investigation of fundamental EMI source mechanisms driving common-mode radiation from printed circuit boards with attached cables," *IEEE Trans. Electromagn. Comp.*, vol. 38, no. 4, pp. 557-565, Nov. 1996.

[15] J. P. Berenger, "Perfectly matched layer for the absorption of electromagnetic waves", *J. Comput. Phys.*, vol. 114, pp. 185-200, Oct. 1994.

[16] D. B. Kuznetsov, and J. E. Schutt-Aine, "Optimal transient simulation of transmission lines", *IEEE Trans. Circuits Syst.*, vol. 43, no. 2, pp. 110-121, Feb. 1996.

[17] Avant! Software Corp., *Star-Hspice Manual*, release 2001.2, June 2001.